BNL-226109-2024-JAAM

Revealing Deformation Mechanisms in Polymer-Grafted Thermoplastic Elastomers via In Situ Small-Angle X-ray Scattering

V. Torres, M. Fukuto

To be published in "ACS Applied Materials & Interfaces"

December 2023

Photon Sciences

Brookhaven National Laboratory

U.S. Department of Energy

USDOE Office of Science (SC), Basic Energy Sciences (BES)

DISCLAIMER

Revealing Deformation Mechanisms in Polymer Grafted Thermoplastic Elastomers *via In Situ* Small-Angle X-Ray Scattering

Vincent M. Torres,[a] Erik Furton,[b] Jensen N. Sevening,[b] Elisabeth C. Lloyd,[b] Masafumi Fukuto,[c] Ruipeng Li,[c] Darren C. Pagan,[b] Allison M. Beese,[b,d,e] Bryan D. Vogt,[f,*] Robert J. Hickey[b,e,*]

[a]Department of Chemistry, The Pennsylvania State University, University Park, Pennsylvania, 16802, United States

[b]Department of Materials Science and Engineering, The Pennsylvania State University, University Park, Pennsylvania, 16802, United States

[c]National Synchrotron Light Source II, Brookhaven National Laboratory, Upton, New York, 11973, United States

[d]Department of Mechanical Engineering, The Pennsylvania State University, University Park, Pennsylvania, 16801, United States

[e]Materials Research Institute, The Pennsylvania State University, University Park, Pennsylvania, 16802, United States

[f]Department of Chemical Engineering, The Pennsylvania State University, University Park, Pennsylvania, 16802, United States

*Corresponding authors: rjh64@psu.edu and bdv5051@psu.edu

Abstract

The tunable properties of thermoplastic elastomers (TPEs), through polymer chemistry manipulations, enable these technologically critical materials to be employed in a broad range of applications. The need to "dial-in" the mechanical properties and responses of TPEs generally requires the design and synthesis of new macromolecules. In these designs, TPEs with nonlinear macromolecular architectures outperform the mechanical properties of their linear copolymer counterparts, but the differences in deformation mechanism providing enhanced performance are unknown. Here, *in situ* small-angle X-ray scattering (SAXS) measurements during uniaxial extension reveal distinct deformation mechanisms between a commercially available linear poly(styrene)-poly(butadiene)-poly(styrene) (SBS) triblock copolymer and the grafted SBS version containing grafted poly(styrene) (PS) chains from the poly(butadiene) (PBD) mid-block. The neat SBS (φ_{SBS} = 100%) sample deforms congruently with the macroscopic dimensions with the domain spacing between spheres increasing and decreasing along and traverse to the stretch direction, respectively. At high extensions, end segment pullout from the PS-rich domains is detected, which is indicated by a disordering of SBS. Conversely, the PS-grafted SBS that is 30 vol% SBS and 70% styrene (φ_{SBS} = 30%) exhibits a lamellar morphology and *in situ* SAXS measurements reveal an unexpected deformation mechanism. During deformation there are two simultaneous processes, significant lamellar domain rearrangement to preferentially orient the lamellae planes parallel to the stretch direction and crazing. The samples whiten at high strains as expected for crazing, which corresponds with the emergence of features in the two-dimensional SAXS pattern during stretching consistent with fibril-like structures that bridge the voids in crazes. The significant domain rearrangement in the grafted copolymers is attributed to the new junctions formed across multiple PS domains by the grafts of a single chain. The *in situ* SAXS measurements

provide insights into the enhanced mechanical properties of grafted copolymers that arise through improved physical crosslinking that leads to nanostructured domain reorientation for self-reinforcement and craze formation where fibrils help to strengthen the polymer.

KEYWORDS: Block Polymers; Nanostructure, *In situ* Measurement; Toughness; Grafted Polymers; Tensile Properties; Crazing

TOC

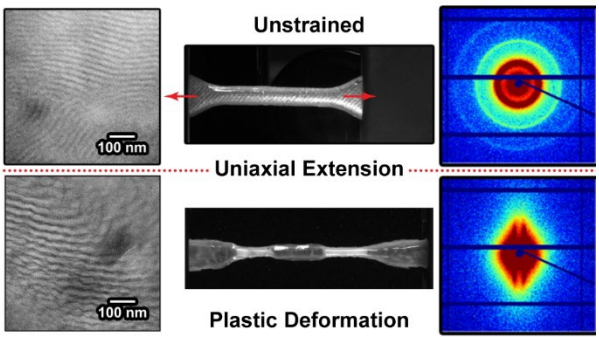

1. Introduction

Thermoplastic elastomers (TPEs) offer performance resembling thermosetting elastomers, while providing the processing flexibility of thermoplastics. These attributes have led to the industrial adoption of TPEs across many applications, with TPEs now utilized in the automotive, construction, medical, and electronic industries.[1,2] The macromolecular architecture of TPEs defines the microphase separated nanostructure, providing physical crosslinks to enable reprocessing and reversible deformation.[3,4] ABA triblock copolymers with hard, glassy polymers as A blocks and the B midblock with a glass transition temperature (T_g) significantly less than the service use temperature provide a simple architecture for a model TPE.[5] The mechanical properties of linear ABA TPEs can be modestly tuned through the chemical composition and the molecular weight, which defines the nanostructure,[6] but adjusting properties through these parameters tend to include tradeoffs with processibility and performance. The performance of linear TPEs can be enhanced with multiblock copolymers with polymer block sequences $(AB)_nA$,[7] ABC[8–10] and ABCBA,[11–13] where domain connectivity through bridging chains helps to improve material toughness but with a drawback, each added block adds costs; this factor has limited the commercial adoption of multiblock copolymer except for some high value applications.[14]

Alternatively, branched polymers, such as miktoarm star block copolymers[15–18] and graft copolymers,[19–23] increase the complexity of the architecture while generally enhancing traditional properties of TPEs.[24–26] Non-linear TPEs exhibit improved mechanical properties as compared to linear TPEs.[27,28] For example, linear poly(l-lactide)-poly(γ-methyl-ε-caprolactone)-poly(l-lactide) (PLLA–PγMCL–PLLA) exhibits lower ultimate tensile strength and toughness than analogous miktoarm star copolymers with similar arm lengths as the linear TPE.[29] Similarly, the tensile strength and Young's modulus of poly(styrene)-poly(butadiene)-poly(styrene) (SBS) TPE are

increased when PS grafts are added to the PBD block *via* post-polymerization modification.[30] A variety of synthetic strategies have been developed for non-linear TPEs, most commonly for miktoarm star polymers[31–33] and multigraft copolymers.[34–36] Multigraft copolymers are of special interest from a customization perspective, as they can be used as a post-polymerization functionalization strategy, specifically in terms of grafting from[37] and grafting to.[35] These techniques open the possibility to chemically modify commercially available TPEs with desired polymer grafts to effectively tune the material properties.

In situ polymer grafting during a polymerization transforms an existing TPE into an effectively new TPE with designer mechanical properties.[30,38,39] One simple route to this modification for SBS is through initiating styrene from PBD *via* allylic hydrogen abstraction from PS grafts.[39] Polymerizing styrene in a PS-PBD diblock copolymer with benzoyl peroxide (BPO) as the radical initiator leads to nanoscale phase transition from a lamellar to a hexagonally packed cylinder morphology, which undergoes a complex phase transition mechanism that has been tracked using *in situ* small-angle X-ray scattering (SAXS) during the polymerization at elevated temperatures.[38] The allylic radical polymer grafting strategy is translatable to linear PBD or triblock SBS, illustrating the universality of this post-polymerization method.[30] Synthesis of non-linear macromolecular architectures is now commonplace, but clear guidance to the design of branched macromolecules as TPE is lacking due to uncertainty regarding why the mechanical properties of the materials are improved over their linear counterparts.

Although grafting PS from commercially available SBS materials increases the Young's modulus (E), the yield stress (YS), and tensile strength (TS) for PS-grafted SBS by >5x and the elongation at break (ε_b) by 2x,[24] the underlying reasons for the enhancement in mechanical properties in the PS-grafted SBS samples are not well understood. Here, the deformation

mechanism of a PS-grafted SBS sample was elucidated using *in situ* SAXS during uniaxial extension to probe nanoscale changes that occur in concert with the macroscopic tensile test. These measurements show differences in the deformation mechanisms of nanostructured TPEs of 1) a commercially available linear SBS triblock copolymer and 2) a grafted version of the SBS containing PS chains from the PBD mid-block (**Figure 1**). The PS grafted SBS responds to tensile deformation after yielding by simultaneously aligning the lamellae domains parallel to the stretching direction and crazing, where fibrils are predicted to bridge the voids, helping to toughen the material. The SAXS profiles for the PS grafted SBS at high strain resemble fibril formation during crazing, which is common in glassy polymers.[40,41] Crazing is further supported by the visual changes in the sample where necking regions turn white. For the neat, linear SBS, the domain reorientation is significantly reduced during deformation and the TPE fails without additional nanostructure formation. These results provide new insights into why non-linear TPEs outperform linear analogs due to mechanistic differences that result from the additional physical crosslinks from the grafts.

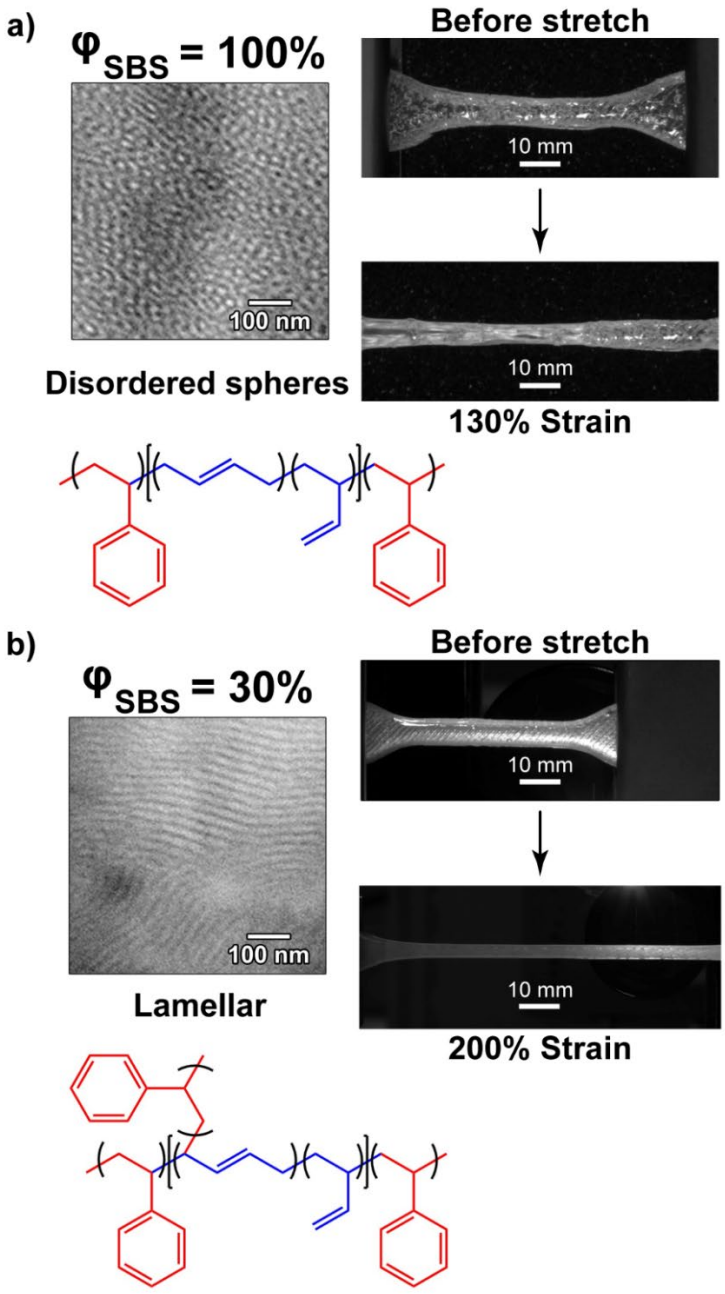

Figure 1. Differences in the nanostructure and deformation of (a) neat SBS (φ_{SBS} = 100%) and (b) PS grafted SBS (φ_{SBS} = 30%). TEM micrographs using OsO_4 staining illustrate the a) disordered sphere morphology in the neat SBS, while b) PS grafted SBS samples form a lamellar morphology. Optical images of unstretched and deformed samples at (a) 130% and (b) 200% strain.

2. Results and Discussion

In situ SAXS during uniaxial extension was used to probe the changes in the nanostructure during deformation for two different TPE samples: 1) a commercially available linear neat SBS sample (φ_{SBS} = 100%) and 2) the linear SBS sample grafted with PS on the PBD mid-block containing 30 volume percent SBS relative to the initial styrene monomer (φ_{SBS} = 30%, which results in a final sample with 77 wt% PS). Synchrotron SAXS is an invaluable method to probe nanoscale changes during nanostructured polymeric material deformation due to its high X-ray flux, which enables real time characterization.[42] The commercially available SBS sample exhibits a disordered sphere morphology, whereas the φ_{SBS} = 30% sample is lamellar (**Figure 1**). Dog bone samples for both samples were prepared from solution using silicone-based molds with ASTM D638 type IV dimensions. The commercially available SBS sample was first dissolved in THF (0.6 g/mL), poured into the mold, dried at room temperature in a fume hood for 12 h, and then vacuum dried at 25 °C for an additional 12 h to remove THF from the sample. Less than 1 wt% THF remains in the sample after vacuum drying as confirmed with ^{1}H NMR (see Supporting Information). Following a previously published procedure,[30] PS-grafted SBS was synthesized by the addition of a solution of SBS (φ_{SBS} = 30%), styrene, and BPO to silicone dog bone mold and subsequent heating at 100 °C for 3 h to polymerize the styrene. PS grafting from the PBD mid-block is initiated from allylic radicals that form when BPO abstracts an allylic hydrogen from a carbon that is adjacent to a vinyl group.[38,39] PS is simultaneously polymerized in the solution, but only 4 wt% of the product was homopolymer as determined from solvent extraction.[30] The grafting reaction leads to a morphology transition from disordered spheres to lamellar as the PS volume fraction of the copolymer is significantly increased from the grafting reaction.

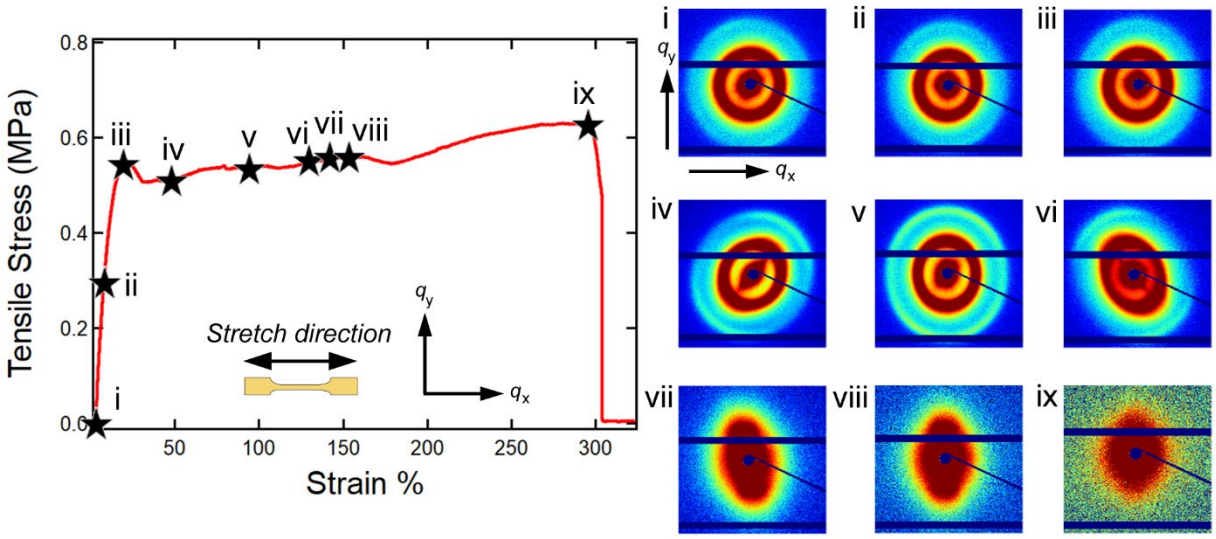

Figure 2. **Engineering stress-strain curve and corresponding 2D SAXS patterns for the neat SBS sample (φ_{SBS} = 100%).** Stars labeled as i – ix on the stress-strain curve correspond to the strains associated with 2D SAXS patterns. Specifically, labels i – ix correspond to 0, 10, 20, 50, 90, 130, 140, 150, and 290%.

Figure 2 shows the stress-strain behavior of the neat SBS (φ_{SBS} = 100%) during tensile deformation on the SAXS beamline. The stress-strain curve in **Figure 2** is consistent with the literature for this commercial SBS where elongation at yield occurs at approximately 20% strain and fracture at strains greater than 100%.[43] The scattering profiles show nearly symmetric concentric rings in the 2D SAXS images at low strain (ε = 0, 10, and 20%, **Figures 2i – iii**). The material should be globally isotropic initially, but there is some initial orientation to the domains that results from the pouring of the concentrated SBS solution into the mold. Interestingly, this asymmetry in the scattering decreases as the specimen is initially stretched (**Figures 2i – iii**). Post yield, there is clear anisotropy in the scattering patterns. At ε = 50% (**Figure 2iv**), the elliptical

scattering pattern however is not aligned, in terms of its major or minor axis, with the stretching direction. Instead, the major axis is aligned at approximately 40° relative to the stretching direction. This tilt is associated with degeneracy in the isotropic nanostructures associated with spherical self-assembly that leads to multiple potential arrangements to respond to applied stresses that decrease the local free energy.[44] As the sample is stretched, the location being probed by the SAXS changes due to a single crosshead moving on the strain stage. Examination of the 2D SAXS patterns at slightly higher strains illustrates how the tilt in the anisotropic 2D scattering patterns changes from location to location (**Figures 2iv – vi)**. At ε = 140, there is a marked change in the scattering patterns with a loss in the peaks associated with a nanostructured material. The scattering remains anisotropic, but the intensity appears to monotonically decay with increasing q. PS end-blocks pullout of the micellar domains at high stresses would result in a "homogenization" of the structure; it is important to note that the weak halo typically present in the scattering for disordered block copolymer systems (correlation hole) is lacking for these materials at high strain.[45] The anisotropic scattering suggest that larger scale features with higher electron contrast than PS-PBD, such as cavitation or crazing,[46–48] overwhelms the scattering from the natural length scale in the block copolymer.

To assess the changes more quantitatively in the nanostructures, the 2D SAXS images in **Figures 2i – ix** were azimuthally integrated over a ±5° sector in the q_x (**Figure 3a**) and q_y (**Figure 3b**) directions. The 1D SAXS profiles illustrate the limited changes in the nanostructure for $\varepsilon \leq 20$ with a minor shift in the primary scattering peak to smaller q for q_x and higher q for q_y. The limited change in the nanostructure indicates that the deformation is not affine, even in the elastic limit. At larger strains ($\varepsilon \geq 50\%$), the primary scattering peak at different strains in **Figures 3a** and 3**b**, emphasized with an asterisk, more clearly shift lower to q in q_x, indicating an increase in the

domain spacing (**Figure 3a**), whereas a shift to higher q in q_y implies a decrease in the micelle center-to-center spacing (**Figure 3b**). Moreover, the 2nd order reflection becomes better defined, which suggests that the nanostructure becomes more ordered at these higher strains. At ε = 130%, there is a significant broadening of the primary scattering peak, but higher order reflections remain in the scattering, which indicates that the sample remains ordered. For $\varepsilon \geq$ 140%, the sample appears to undergo a disordering process that is inferred by a decrease in intensity and broadening of the primary scattering peak.

The SAXS patterns for the neat SBS sample were further analyzed by fitting the 1D patterns in the q_x and q_y directions with a spheroid form factor and a hard sphere structure factor derived from the Percus-Yevick approximation. An example of the fit for the undeformed neat SBS sample in the q_x direction is shown in **Figure 3c**, indicating that the fit matches the experimental data over a large q-range and the fit supports the disordered sphere morphology classification. Additional fits of these SAXS patterns of the neat SBS are in the Supporting Information. The micelle-to-micelle distance (i.e., domain spacing (d)) values from the SAXS fits with standard deviation are plotted versus strain and shown in **Figure 3d**. As expected from the 1D SAXS patterns, there is minimal to no change in the domain spacing at low strains (e.g., $\varepsilon \leq$ 20). When $\varepsilon \geq$ 50%, the domain spacing increases in q_x whereas the domain spacing decreases in q_y. Furthermore, the size of the scatterers (i.e., PS spheres) is constant in both the q_x and q_z directions up until $\varepsilon \approx$ 120%, indicating that the spheres do not change during deformation in the low strain regions (see Supporting Information).

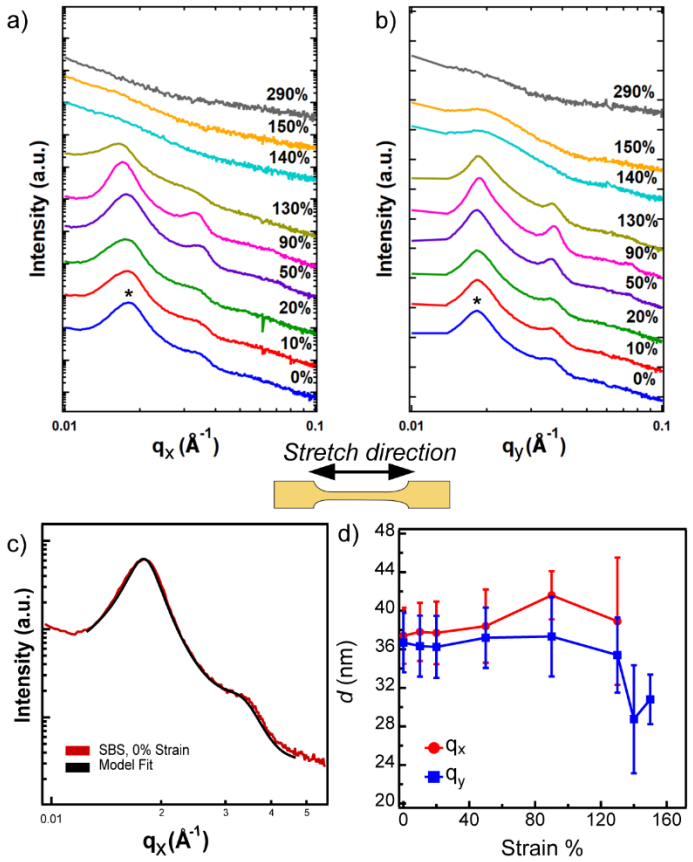

Figure 3. 1D SAXS profiles for neat SBS (φ_{SBS} = 100%) sample in the (a) q_x and (b) q_y directions. The asterisk (*) indicates the primary scattering peak position. (c) 1D SAXS plot with a spheroid form factor and a hard sphere structure factor derived from the Percus-Yevick approximation fit for the undeformed neat SBS sample in the q_x direction. (d) Plot indicating the change in domain spacing with respect to strain in q_x and q_y directions. The domain spacing values with standard deviation were determined from the SAXS fits.

In comparison, the φ_{SBS} = 30% sample exhibits a drastically different nanoscale deformation process (**Figure 4**). As previously reported, these grafted SBS copolymers exhibit increased Young's modulus (E), yield stress (YS), tensile strength (TS), and elongation at break

(ε_b) in comparison to the initial linear SBS.[30] As shown in **Figure 4**, the ultimate tensile strength for the φ_{SBS} = 30% sample is an order of magnitude greater than the φ_{SBS} = 100% sample (**Figure 2**), which can be explained by the increased PS content but addition of PS should also embrittle the grafted copolymer but this is not observed. Understanding the nanoscale deformation mechanisms will provide insights into how both strength and ductility are simultaneously increased. At low strains (ε < 25%), the scattering patterns are nearly symmetric with uniform azimuthal intensity, confirming that the lamellar domains are initially randomly oriented. Increasing the strain from 25 to 75%, within the plastic deformation region, the 2D SAXS patterns become anisotropic in both q and azimuthal intensity, indicating that the lamellar domains are becoming oriented. Strikingly, the *in situ* 2D SAXS transition from a ring to an arc associated with the lamellae planes aligning parallel to the stretch direction to two distinct maxima for ε = 100 – 325% (**Figures 4vi** – **viii**). The 2D SAXS patterns in **Figures 4vi** – **viii** resemble the SAXS patterns of glassy polymers that form crazes during deformation.[40,41] If only grain reorientation was present, the drastic changes in **Figures 4vi** – **viii** would not be present. The clear loss of only higher order reflections at higher strains are indicative of a substantial change in the morphology. Although similar scattering patterns can evolve in linear block copolymers,[49] there are key differences associated with these graft copolymers. Prior work used pre-aligned block polymers and only when the lamellae planes were oriented perpendicular to the deformation did similar scattering evolve from the formation of chevon-like patterns from defects induced in the lamellae on stretching normal to the oriented plane. Here, we find that the graft copolymers orient preferentially with the lamellae planes parallel to the deformation direction; this orientation is induced by stretching as the initial sample is effectively isotropic. This difference in orientation of the lamellae between the previously reported linear block polymers (perpendicular) and here for the graft copolymer

(parallel) suggests a difference in the mechanism for the re-orientation at high strain. Based on these differences, we hypothesize that the 2D SAXS patterns in **Figures 4vi** – **viii** suggest fibril formation in the PS-grafted SBS system, which is facilitated by the macromolecular architecture and the higher PS content that enables crazing.

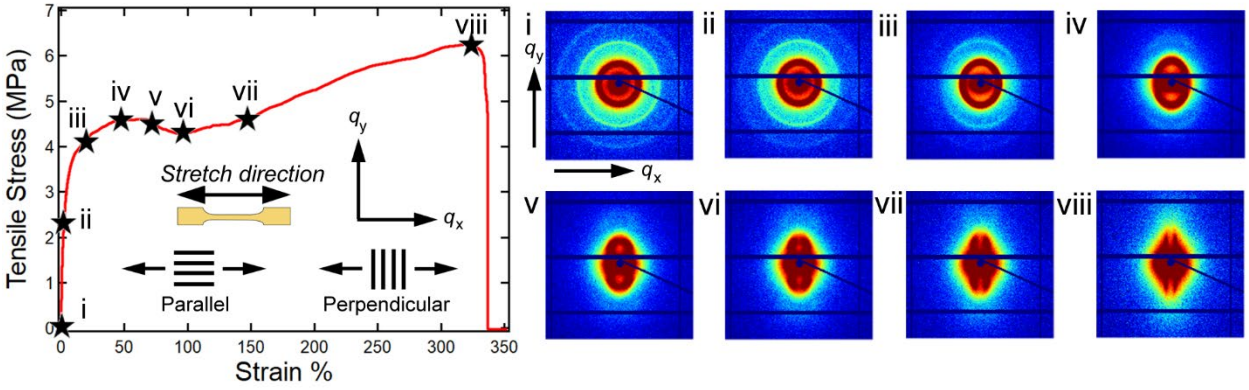

Figure 4. **Engineering stress-strain curve and 2D *in situ* SAXS patterns for the φ_{SBS} = 30% sample.** Stars labeled as i – viii on the stress-strain curve correspond to the strains associated with 2D SAXS patterns. Specifically, labels i – viii correspond to 0, 10, 25, 50, 75, 100, 160, and 325%.

As in the neat SBS sample (φ_{SBS} = 100%), the 2D SAXS patterns in **Figures 4vi** – **viii** for the φ_{SBS} = 30% sample were azimuthally integrated in the q_x (**Figure 5a**) and the q_y (**Figure 5b**) directions. The 1D plots show that the primary scattering peaks in both q_x and q_y significantly broaden after the yield point (ε > 25%). Furthermore, there is a shift to lower q in q_x (**Figure 5a**) and a shift to higher q in q_y (**Figure 5a**), which is consistent with the changes in the macroscopic dimensions during uniaxial extension. Similar trends have been reported for the deformation of

poly(methyl methacrylate)-poly(n-butyl acrylate)/poly(methyl methacrylate)-poly(n-butyl acrylate)-poly(methyl methacrylate) diblock and triblock copolymer blends, where the domain spacing in the loading direction increased whereas the domain spacing in the transverse direction decreased during uniaxial extension.[50] Comparison of the scattering profiles in q_x and q_y illustrates the alignment of the lamellae during deformation at 10 and 25% strain; the primary peak is sharper in q_y and the 2nd order reflection is also better defined. It is important to note that the scattering from the lamellae arises from correlations normal to the plane, so the increased scattering intensity in **Figure 5b** is associated with the lamellae planes aligning parallel to the stretching direction. The primary peak is not well resolved in q_x beginning at 50% strain, while multiple peaks appear in the SAXS profile in q_y at 160% strain. For the latter, the peaks at these higher strains broaden significantly and shift to higher q, which indicates a thinning of the lamellae as the chains are stretched with a broader distribution in the spacing. These changes in q for the primary scattering peak, in addition to the domain spacing, $d = 2\pi/q^*$, in q_x and q_y are shown in **Figure 5c** and **d**. Specifically, there is a drastic change in the slope for strains in the plastic regime (e.g., $\varepsilon \geq 25\%$), signifying that the nanoscale structure deformation is dependent on the orientation of the lamellae relative to the deformation direction. The increased change in q_x scattering (associated with perpendicular alignment of the lamellae planes to the stretching direction) is consistent with the reorientation of the domains as these perpendicularly oriented lamellae are effectively torn apart by the deformation.

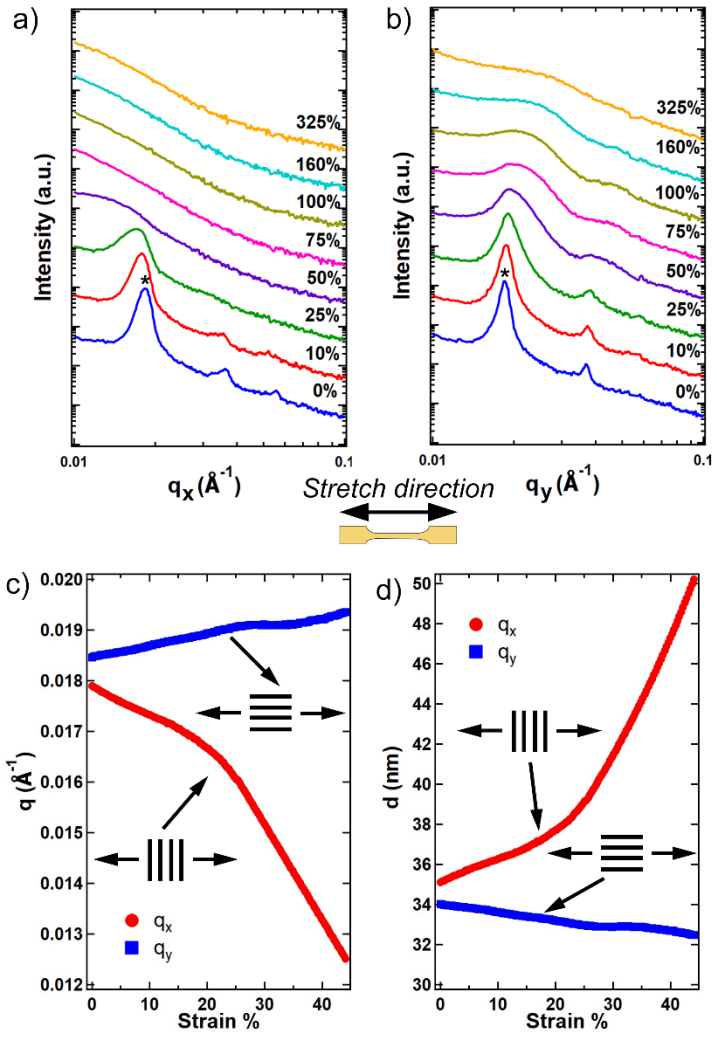

Figure 5. 1D SAXS plots for the φ_{SBS} = 30% in the (a) parallel and (b) perpendicular directions with respect to applied tensile load. Impact of strain on the (c) *q*-value and (d) domain spacing for the primary scattering peak in the loading (red) and transverse (blue) direction.

The results presented in **Figures 2 – 5** support that claim that the φ_{SBS} = 100% and φ_{SBS} = 30% samples exhibit different deformations mechanisms in the plastic regime when uniaxially stretched. *In situ* optical imaging during uniaxial extension highlights the drastic differences (**Figure 6**). Both samples deform similarly in the elastic regime, which consists of stretching the

low T_g PBD domains. The preferred deformation mechanism in the plastic region at high strains for the φ_{SBS} = 100% sample is predicted to be chain pullout, although cavitation or crazing are possible and have been shown to occur in block copolymer systems.[46–48] The PS-grafted SBS sample (φ_{SBS} = 30%) is expected to undergo two simultaneous processes: lamellar domain reorientation and crazing (**Figure 6**). A white region at the neck, indicating crazing, for the φ_{SBS} = 30% sample occurs directly after the yield point. As the sample is continually deformed, the craze region increases. The specific φ_{SBS} = 30% sample shown in **Figure 6** forms two independent craze regions. Videos showing the deformation process for the φ_{SBS} = 100% and 30% samples are in the Supplementary Information.

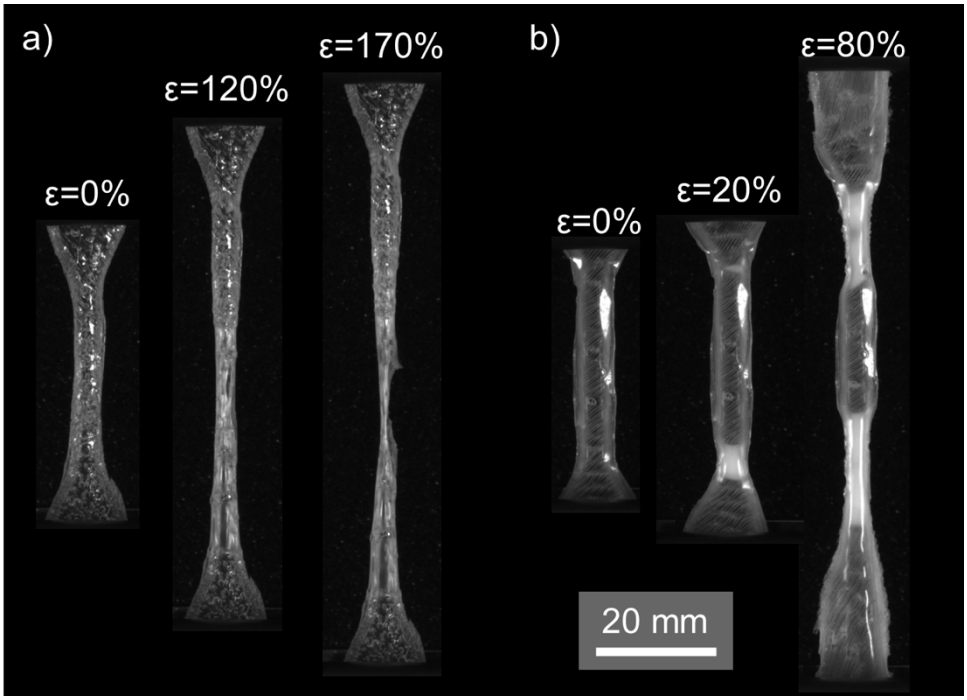

Figure 6. *In situ* optical images during uniaxial extension for (a) φ_{SBS} = 100% and (b) φ_{SBS} = 30% samples. The two samples undergo substantially different deformation mechanisms. The φ_{SBS} = 30% sample exhibits a crazing process as indicated by the formation of white regions. Videos showing the deformation process for both samples are in the Supplementary Information.

The reason for the drastic changes in the plastic regime between the two samples is the difference in macromolecular architecture. The PS grafts in the φ_{SBS} = 30% sample reside in the PS domains, forming multiple additional junctions per chain. These junctions act to anchor the chain as the cooperativity in chain pull out is increased to fully free a single copolymer chain and thus favors domain reorientation. For example, when the sample is stretched in the plastic regime, there is likely chain pull out of grafts from the PS domains, but the presence of additional junctions enables further domain reorientation due to the elasticity that results from the remaining junctions. Furthermore, the additional PS junctions are predicted to assist fibril formation that bridge crazes, similarly to glassy polymers and block copolymer systems.[40,41,46–48,51] An alternative interpretation of the deformation mechanism for the φ_{SBS} = 30% sample is that in the plastic regime, the glassy PS lamellar domains break up and form "chevron" structures, which has been reported in oriented PS-PBD-PS and poly(styrene)-poly(ethylene-co-butylene)-poly(styrene) (SEBS) lamellar samples, but this breakup mechanism was only observed with perpendicular orientation of the lamellae.[52] TEM images in the fracture region confirm that "chevron" structures do not form during deformation (**Figure 7**). As seen in the TEM images, the lamellar nanostructure is highly deformed, and the nanoscale domains are wrinkled. The distinction between the PS-grafted sample reported here and the previous reports is that adding additional polymer junctions by controlling macromolecular architecture opens new deformation mechanisms and design rules for tailoring mechanical properties.

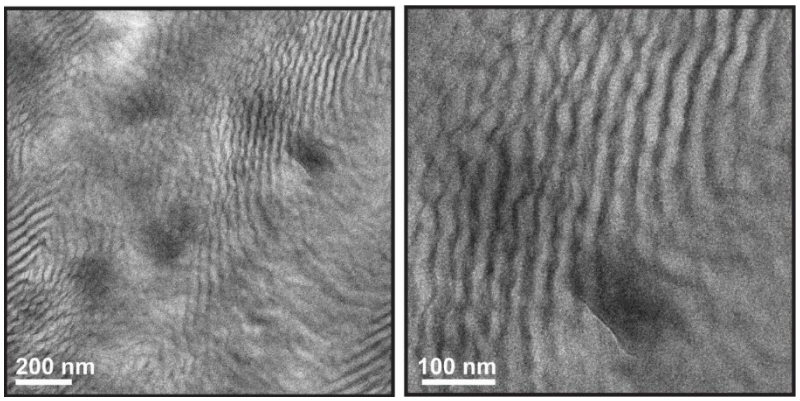

Figure 7. TEM images of the fracture region for the φ_{SBS} = 30% sample. TEM samples were prepared by microtoming the sample in the fracture region parallel to the stretch direction and then staining with OsO_4.

3. Conclusion

Macromolecular architecture is a critical tuning parameter in controlling block copolymer nanostructure and mechanical properties. Here, *in situ* SAXS and optical imaging during uniaxial extension reveal two drastically different deformation mechanisms between the linear SBS TPE and PS-grafted SBS samples. The neat SBS (φ_{SBS} = 100%) sample, consisting of a disordered sphere morphology, demonstrates nanoscale deformation where the sphere center-to-center distance increases in q_x and decreases in q_y while in the elastic regime. At high extensions, it is predicted that the PS end-blocks pullout from the PS-rich domains, leading to a decrease in the intensity of the primary SAXS peak and a less defined nanostructure. In contrast, the PS-grafted SBS φ_{SBS} = 30% sample, exhibiting a lamellar morphology, undergo significant lamellar domain rearrangement to preferentially orient the lamellae plane with the stretch direction and the emergence of crazes. As the strain increases, the 2D SAXS patterns suggest the formation of fibrils, which is consistent with crazes. The stark difference in deformation processes between the two

samples are attributed to the macromolecular architecture where the PS-grafts in the φ_{SBS} = 30% sample lead to cooperativity due to the new junctions formed across PS domains by the grafts. The new insights revealed through *in situ* SAXS and optical imaging during uniaxial extension measurements of linear and grafted copolymer materials will guide future design rules for tailoring desired mechanical properties and deformation responses.

4. Experimental

4.1 Materials

Poly(styrene)-poly(butadiene)-poly(styrene) (SBS) triblock copolymer (styrene 30 wt%, CAS Number: 308076-12-2) and benzoyl peroxide (BPO) (regent grade, ≥ 98%) were purchased from Sigma Aldrich (St. Louis, USA) and used as received. Tetrahydrofuran (THF) (HPLC grade) was purchased from ThermoFisher Scientific (Waltham, USA). Aluminum oxide powder was purchased from Honeywell (Charlotte, USA). Styrene monomer (≥ 99%) was purchased from Sigma Aldrich (St. Louis, USA) and purified *via* aluminum oxide to remove inhibitor. The tin-cure silicone rubber mold mixture for the mold, OOMOO™ 30 was purchased from Smooth-on (Macungie, USA).

4.2 Silicone Mold Preparation

To prepare the silicone mold, samples of ASTM standard D638 type IV dog bones were 3D printed (3D Hubs, 115 x 19 x 4 mm). These dog bones were then laid across packing tape that lined the bottom of a disposable aluminum baking pan. The OOMOO™ 30 tin-cure silicone was prepared, and then poured over the dog bones. The resulting mold was cured for 6 hours at 25 °C then placed in an oven for 4 h at 65 °C.

4.3 Dog Bone Sample Preparation

Styrene was purified by passing it through a column of aluminum oxide to remove any inhibitor in the monomer. SBS was dissolved in styrene monomer at a volume fraction of 30% until homogenous. BPO was then added (100:1 styrene to BPO) and mixed. Triblock copolymer/monomer blends were added to a silicone dog bone mold and placed in an oven at 100 °C for 3 h to graft PS onto the SBS. The $\varphi_{SBS} = 100\%$ dog bones were prepared by dissolving SBS in THF (0.6 g/mL), followed by injection *via* syringe into the mold. THF was partially evaporated from the sample by placing in a fume hood for 24 h. All dog bones were subject to a low vacuum for 12 h at 25 °C to remove unreacted monomer or solvent.

4.4 Transmission Electron Microscopy (TEM)

Micrographs of the dog bone samples were obtained using a FEI Tecnai G2 Spirit BioTwin TEM. Samples were prepared by microtoming dog bone samples (approximately 70-90 nm thick sections using a Leica UC6 ultramicrotome), placing the microtomed samples onto TEM grids (Electron Microscopy Sciences, Formvar/Carbon 200 Mesh, Copper), and staining the samples with osmium tetroxide vapor for 15 min to distinguish between the PS and PBD domains.[53]

4.5 *In situ* Tensile/SAXS

SAXS measurements were conducted at the National Synchrotron Light Source II (NSLS-II) at Brookhaven National Laboratory using the Complex Materials Scattering (CMS/11-BM) beamline. For *in-situ* tensile test during SAXS measurements, a Linkam strain stage with a 200 N loadcell was used as described previously.[54] Samples were cut to be 25 x 2 x 1 mm and were

mounted between the load frame grips with a gauge length of 15 mm. Samples were strained at a rate of 1.8 mm/min. During the tensile test, every 4 s the samples were exposed for 10 s using a 13.50 keV (λ =0.9184 Å) beam. A sample to detector distance of 2 m was used to probe the q-range from 0.008–0.444 $Å^{-1}$. Scattering images were captured with a Dectris Pilatus 2M detector (pixel size 172 μm × 172 μm). The 2D scattering data were corrected for background using scattering in air as the reference.

1D scattering profiles were obtained from the 2D scattering patterns using the IRENA package obtained as an open resource from Argonne National Lab in Igor Pro 8.[55] The q^* values for both parallel and perpendicular to the loading directions for the φ_{SBS} = 30% sample were determined by first integrating ±5° azimuthal bins along 0° and 90° directions relative to the deformation of the tensile test to generate 1D line profiles. After azimuthal integration, symmetric pseudo-Voigt peak functions were fit to primary peaks along with a linear background. The q^* at each strain was assumed to be the peak position of the pseudo-Voigt fit.

SAXS data for the pure SBS polymer—showing disordered sphere morphology in the neat state—were fit using IRENA. The data were fit with a spheroid form factor and a hard sphere structure factor derived from the Percus-Yevick approximation. The micelle diameter and standard deviation, the domain spacing (micelle center-to-center distance), and the volume fraction of scatterers were used as fitting parameters. The fitting region was confined to the primary peak and immediate surroundings to avoid scattering from heterogeneity of the sample at low q and background at high q from affecting the fit results.

4.6 Optical Microscopy

To quantify macroscopic deformation behavior, samples were loaded in uniaxial tension with an electromechanical load frame (MTS Criterion Model 45) at a constant displacement rate of 0.08 mm/s, for an engineering strain rate of approximately 3×10^{-3} mm/s. Images were taken with a digital camera (GRAS-50S5M-C, FLIR, Wilsonville, OR).

ASSOCIATED CONTENT

The Supporting Information is available free of charge at https://pubs.acs.org.

1D SAXS fits for the undeformed and strained neat SBS sample; plot of the SAXS fitting parameters; ^{1}H NMR; videos of *in situ* optical imaging

AUTHOR INFORMATION

Corresponding Authors

Robert J. Hickey (rjh64@psu.edu) and Bryan D. Vogt (bdv5051@psu.edu)

ORCID

Vincent M. Torres: 0000-0003-0171-0664

Erik Furton: 0000-0002-1471-2813

Jensen N. Sevening: 0000-0002-1934-0617

Elisabeth C. Lloyd: 0000-0003-1423-6463

Masafumi Fukuto:

Ruipeng Li:

Darren C. Pagan: 0000-0001-8638-6546

Allison M. Beese: 0000-0002-7022-3387

Bryan D. Vogt: 0000-0003-1916-7145

Robert J. Hickey: 0000-0001-6808-7411

Notes

The authors declare no competing financial interest.

ACKNOWLEDGMENTS

This work was supported by the National Science Foundation (NSF), Division of Materials Research (DMR), Polymers Program (CAREER Proposal No.: DMR-1942508) and the National Science Foundation Graduate Research Fellowship under Grant No. DGE1255832. The SAXS results were acquired at the Complex Materials Scattering beamline of the National Synchrotron Light Source II, a U.S. Department of Energy (DOE) Office of Science User Facility operated for the DOE Office of Science by Brookhaven National Laboratory under Contract No. DE-SC0012704. TEM measurements were conducted at the Materials Characterization Lab (MCL) in the Materials Research Institute (MRI) at the Pennsylvania State University. We are grateful to Missy Hazen for her help with microtoming and staining the polymer samples for TEM.

References

(1) Spontak, R. J.; Patel, N. P. Thermoplastic Elastomers: Fundamentals and Applications. *Curr Opin Colloid Interface Sci* **2000**, *5* (5–6), 333–340. https://doi.org/10.1016/S1359-0294(00)00070-4.

(2) Morton, M.; McGrath, J. E.; Juliano, P. C. Structure-Property Relationships for Styrene-Diene Thermoplastic Elastomers. *Journal of Polymer Science Part C: Polymer Symposia* **2007**, *26* (1), 99–115. https://doi.org/10.1002/polc.5070260107.

(3) Holden, G. Elastomers, Thermoplastic. In *Encyclopedia of Polymer Science and Technology*; Mark, H. F., Kroschwitz, J. I., Eds.; John Wiley & Sons: Hoboken, 2004; Vol. 6, pp 63–88.

(4) Stadler, R.; Gronski, W. Effects of Phase Separation on Network and Viscoelastic Properties in SBS Thermoplastic Elastomers. *Colloid Polym Sci* **1983**, *261* (3), 215–223. https://doi.org/10.1007/BF01469666.

(5) Puskas, J. E.; Kaszas, G. Polyisobutylene-Based Thermoplastic Elastomers: A Review. *Rubber Chemistry and Technology* **1996**, *69* (3), 462–475. https://doi.org/10.5254/1.3538381.

(6) Holden, G.; Bishop, E. T.; Legge, N. R. Thermoplastic Elastomers. *Journal of Polymer Science Part C: Polymer Symposia* **2007**, *26* (1), 37–57. https://doi.org/10.1002/polc.5070260104.

(7) Barent, R. D.; Perevyazko, I.; Mikusheva, N.; Floudas, G.; Frey, H. Linear (IS) $_n$ I Multiblock Copolymers: Tailoring the Softness of Thermoplastic Elastomers by Flexible Polyisoprene End Blocks. *Macromolecules* **2023**, *56* (15), 5792–5802. https://doi.org/10.1021/acs.macromol.3c00513.

(8) Schmalz, H.; Böker, A.; Lange, R.; Krausch, G.; Abetz, V. Synthesis and Properties of ABA and ABC Triblock Copolymers with Glassy (A), Elastomeric (B), and Crystalline (C) Blocks. *Macromolecules* **2001**, *34* (25), 8720–8729. https://doi.org/10.1021/ma010875d.

(9) Schmalz, H.; Abetz, V.; Lange, R. Thermoplastic Elastomers Based on Semicrystalline Block Copolymers. *Compos Sci Technol* **2003**, *63* (8), 1179–1186. https://doi.org/10.1016/S0266-3538(03)00039-3.

(10) Yamaguchi, D.; Cloitre, M.; Panine, P.; Leibler, L. Phase Behavior and Viscoelastic Properties of Thermoplastic Elastomer Gels Based on ABC Triblock Copolymers. *Macromolecules* **2005**, *38* (18), 7798–7806. https://doi.org/10.1021/ma050294e.

(11) Hirata, M.; Masutani, K.; Kimura, Y. Synthesis of ABCBA Penta Stereoblock Polylactide Copolymers by Two-Step Ring-Opening Polymerization of <scp>l</Scp> - and <scp>d</Scp> -Lactides with Poly(3-Methyl-1,5-Pentylene Succinate) as Macroinitiator (C): Development of Flexible Stereocomplexed Polylactide Materials. *Biomacromolecules* **2013**, *14* (7), 2154–2161. https://doi.org/10.1021/bm400228x.

(12) Burns, A. B.; Register, R. A. Thermoplastic Elastomers via Combined Crystallization and Vitrification from Homogeneous Melts. *Macromolecules* **2016**, *49* (1), 269–279. https://doi.org/10.1021/acs.macromol.5b02546.

(13) Nishiwaki, Y.; Masutani, K.; Kimura, Y.; Lee, C. Synthesis and Mechanochemical Properties of Biobased <scp>ABCBA</Scp> -type Pentablock Copolymers

Comprising Poly- <scp>d</Scp> -lactide (A), Poly- <scp>l</Scp> -lactide (B) and Poly(1,2-propylene Succinate) (C). *Journal of Polymer Science* **2022**, *60* (14), 2043–2054. https://doi.org/10.1002/pol.20210883.

(14) Madathil, K.; Lantz, K. A.; Stefik, M.; Stein, G. E. Effects of Trace Water on Self-Assembly of Sulfonated Block Copolymers During Solution Processing. *ACS Appl Polym Mater* **2020**, *2* (11), 4893–4901. https://doi.org/10.1021/acsapm.0c00806.

(15) Juhari, A.; Mosnáček, J.; Yoon, J. A.; Nese, A.; Koynov, K.; Kowalewski, T.; Matyjaszewski, K. Star-like Poly (n-Butyl Acrylate)-b-Poly (α-Methylene-γ-Butyrolactone) Block Copolymers for High Temperature Thermoplastic Elastomers Applications. *Polymer (Guildf)* **2010**, *51* (21), 4806–4813. https://doi.org/10.1016/j.polymer.2010.08.017.

(16) Dufour, B.; Tang, C.; Koynov, K.; Zhang, Y.; Pakula, T.; Matyjaszewski, K. Polar Three-Arm Star Block Copolymer Thermoplastic Elastomers Based on Polyacrylonitrile. *Macromolecules* **2008**, *41* (7), 2451–2458. https://doi.org/10.1021/ma702561b.

(17) Spencer, R. K. W.; Matsen, M. W. Domain Bridging in Thermoplastic Elastomers of Star Block Copolymer. *Macromolecules* **2017**, *50* (4), 1681–1687. https://doi.org/10.1021/acs.macromol.7b00078.

(18) Shi, W.; Lynd, N. A.; Montarnal, D.; Luo, Y.; Fredrickson, G. H.; Kramer, E. J.; Ntaras, C.; Avgeropoulos, A.; Hexemer, A. Toward Strong Thermoplastic Elastomers with Asymmetric Miktoarm Block Copolymer Architectures. *Macromolecules* **2014**, *47* (6), 2037–2043. https://doi.org/10.1021/ma402566g.

(19) Zhang, J.; Keith, A. N.; Sheiko, S. S.; Wang, X.; Wang, Z. To Mimic Mechanical Properties of the Skin by Inducing Oriented Nanofiber Microstructures in Bottlebrush Cellulose- *Graft* -Diblock Copolymer Elastomers. *ACS Appl Mater Interfaces* **2021**, *13* (2), 3278–3286. https://doi.org/10.1021/acsami.0c21494.

(20) Zhang, J.; Wang, Z.; Wang, X.; Wang, Z. The Synthesis of Bottlebrush Cellulose-*Graft* -Diblock Copolymer Elastomers *via* Atom Transfer Radical Polymerization Utilizing a Halide Exchange Technique. *Chemical Communications* **2019**, *55* (92), 13904–13907. https://doi.org/10.1039/C9CC06982H.

(21) Wang, Z.; Yuan, L.; Jiang, F.; Zhang, Y.; Wang, Z.; Tang, C. Bioinspired High Resilient Elastomers to Mimic Resilin. *ACS Macro Lett* **2016**, *5* (2), 220–223. https://doi.org/10.1021/acsmacrolett.5b00843.

(22) Wang, Z.; Jiang, F.; Zhang, Y.; You, Y.; Wang, Z.; Guan, Z. Bioinspired Design of Nanostructured Elastomers with Cross-Linked Soft Matrix Grafting on the Oriented Rigid Nanofibers To Mimic Mechanical Properties of Human Skin. *ACS Nano* **2015**, *9* (1), 271–278. https://doi.org/10.1021/nn506960f.

(23) Jiang, F.; Wang, Z.; Qiao, Y.; Wang, Z.; Tang, C. A Novel Architecture toward Third-Generation Thermoplastic Elastomers by a Grafting Strategy. *Macromolecules* **2013**, *46* (12), 4772–4780. https://doi.org/10.1021/ma4007472.

(24) Weidisch, R.; Gido, S. P.; Uhrig, D.; Iatrou, H.; Mays, J.; Hadjichristidis, N. Tetrafunctional Multigraft Copolymers as Novel Thermoplastic Elastomers. *Macromolecules* **2001**, *34* (18), 6333–6337. https://doi.org/10.1021/ma001966y.

(25) Wang, H.; Lu, W.; Wang, W.; Shah, P. N.; Misichronis, K.; Kang, N.; Mays, J. W. Design and Synthesis of Multigraft Copolymer Thermoplastic Elastomers: Superelastomers. *Macromol Chem Phys* **2018**, *219* (1), 1700254. https://doi.org/10.1002/macp.201700254.

(26) Jiang, F.; Pan, C.; Zhang, Y.; Fang, Y. Cellulose Graft Copolymers toward Strong Thermoplastic Elastomers via RAFT Polymerization. *Appl Surf Sci* **2019**, *480*, 162–171. https://doi.org/10.1016/j.apsusc.2019.02.210.

(27) Zhu, Y.; Burgaz, E.; Gido, S. P.; Staudinger, U.; Weidisch, R.; Uhrig, D.; Mays, J. W. Morphology and Tensile Properties of Multigraft Copolymers with Regularly Spaced Tri-, Tetra-, and Hexafunctional Junction Points. *Macromolecules* **2006**, *39* (13), 4428–4436. https://doi.org/10.1021/ma060067s.

(28) Staudinger, U.; Weidisch, R.; Zhu, Y.; Gido, S. P.; Uhrig, D.; Mays, J. W.; Iatrou, H.; Hadjichristidis, N. Mechanical Properties and Hysteresis Behaviour of Multigraft Copolymers. *Macromol Symp* **2006**, *233* (1), 42–50. https://doi.org/10.1002/masy.200690027.

(29) Liffland, S.; Hillmyer, M. A. Enhanced Mechanical Properties of Aliphatic Polyester Thermoplastic Elastomers through Star Block Architectures. *Macromolecules* **2021**, *54* (20), 9327–9340. https://doi.org/10.1021/acs.macromol.1c01357.

(30) Torres, V. M.; LaNasa, J. A.; Vogt, B. D.; Hickey, R. J. Controlling Nanostructure and Mechanical Properties in Triblock Copolymer/Monomer Blendsviareaction-Induced Phase Transitions. *Soft Matter* **2021**, *17* (6), 1505–1512. https://doi.org/10.1039/d0sm01661f.

(31) Tunca, U.; Ozyurek, Z.; Erdogan, T.; Hizal, G. Novel Miktofunctional Initiator for the Preparation of an ABC-Type Miktoarm Star Polymer via a Combination of Controlled Polymerization Techniques. *J Polym Sci A Polym Chem* **2004**, *42* (17), 4228–4236. https://doi.org/10.1002/pola.20284.

(32) Gao, H.; Matyjaszewski, K. Structural Control in ATRP Synthesis of Star Polymers Using the Arm-First Method. *Macromolecules* **2006**, *39* (9), 3154–3160. https://doi.org/10.1021/ma060223v.

(33) Urbani, C. N.; Bell, C. A.; Whittaker, M. R.; Monteiro, M. J. Convergent Synthesis of Second Generation AB-Type Miktoarm Dendrimers Using “Click” Chemistry

Catalyzed by Copper Wire. *Macromolecules* **2008**, *41* (4), 1057–1060. https://doi.org/10.1021/ma702707e.

(34) Hansson, S.; Trouillet, V.; Tischer, T.; Goldmann, A. S.; Carlmark, A.; Barner-Kowollik, C.; Malmström, E. Grafting Efficiency of Synthetic Polymers onto Biomaterials: A Comparative Study of Grafting- *from* versus Grafting- *To*. *Biomacromolecules* **2013**, *14* (1), 64–74. https://doi.org/10.1021/bm3013132.

(35) Zdyrko, B.; Luzinov, I. Polymer Brushes by the "Grafting to" Method. *Macromol Rapid Commun* **2011**, *32* (12), 859–869. https://doi.org/10.1002/marc.201100162.

(36) Hadjichristidis, N.; Pitsikalis, M.; Iatrou, H.; Pispas, S. The Strength of the Macromonomer Strategy for Complex Macromolecular Architecture: Molecular Characterization, Properties and Applications of Polymacromonomers. *Macromol Rapid Commun* **2003**, *24* (17), 979–1013. https://doi.org/10.1002/marc.200300050.

(37) Liu, Y.; Klep, V.; Zdyrko, B.; Luzinov, I. Polymer Grafting via ATRP Initiated from Macroinitiator Synthesized on Surface. *Langmuir* **2004**, *20* (16), 6710–6718. https://doi.org/10.1021/la049465j.

(38) Zofchak, E. S.; Lanasa, J. A.; Torres, V. M.; Hickey, R. J. Deciphering the Complex Phase Behavior during Polymerization- Induced Nanostructural Transitions of a Block Polymer/Monomer Blend. *Macromolecules* **2020**, *53*, 835–843. https://doi.org/10.1021/acs.macromol.9b01695.

(39) Zofchak, E. S.; Lanasa, J. A.; Mei, W.; Hickey, R. J. Polymerization-Induced Nanostructural Transitions Driven by in Situ Polymer Grafting. *ACS Macro Lett* **2018**, *7* (7), 822–827. https://doi.org/10.1021/acsmacrolett.8b00378.

(40) Brown, H. R.; Mills, P. J.; Kramer, E. J. A SAXS Study of a Single Crack and Craze in Plasticized Polystyrene. *Journal of Polymer Science: Polymer Physics Edition* **1985**, *23* (9), 1857–1867. https://doi.org/10.1002/pol.1985.180230910.

(41) Brown, H. R.; Kramer, E. J. Craze Microstructure from Small-Angle x-Ray Scattering (SAXS). *Journal of Macromolecular Science, Part B* **1981**, *19* (3), 487–522. https://doi.org/10.1080/00222348108015315.

(42) Dencheva, N.; Stribeck, A.; Denchev, Z. Nanostructure Development in Multicomponent Polymer Systems Characterized by Synchrotron X-Ray Scattering. *Eur Polym J* **2016**, *81*, 447–469. https://doi.org/10.1016/j.eurpolymj.2016.02.004.

(43) Diamant, J.; Soong, D.; Williams, M. C. The Mechanical Properties of Styrene-Butadiene-Styrene (SBS) Triblock Copolymer Blends with Polystyrene (PS) and Styrene-Butadiene Copolymer (SBR). *Polym Eng Sci* **1982**, *22* (11), 673–683. https://doi.org/10.1002/pen.760221104.

(44) Xue, J.; Singh, G.; Qiang, Z.; Karim, A.; Vogt, B. D. Unidirectional Self-Assembly of Soft Templated Mesoporous Carbons by Zone Annealing. *Nanoscale* **2013**, *5* (17), 7928. https://doi.org/10.1039/c3nr02821f.

(45) Bates, F. S.; Rosedale, J. H.; Fredrickson, G. H. Fluctuation Effects in a Symmetric Diblock Copolymer near the Order–Disorder Transition. *J Chem Phys* **1990**, *92* (10), 6255–6270. https://doi.org/10.1063/1.458350.

(46) Schwier, C. E.; Argon, A. S.; Cohen, R. E. Craze Plasticity in a Series of Polystyrene/Polybutadiene Di-Block Copolymers with Spherical Morphology. *Philosophical Magazine A* **1985**, *52* (5), 581–603. https://doi.org/10.1080/01418618508237650.

(47) Declet-Perez, C.; Francis, L. F.; Bates, F. S. Cavitation in Block Copolymer Modified Epoxy Revealed by In Situ Small-Angle X-Ray Scattering. *ACS Macro Lett* **2013**, *2* (10), 939–943. https://doi.org/10.1021/mz4004419.

(48) Liu, J. (Daniel); Sue, H.-J.; Thompson, Z. J.; Bates, F. S.; Dettloff, M.; Jacob, G.; Verghese, N.; Pham, H. Nanocavitation in Self-Assembled Amphiphilic Block Copolymer-Modified Epoxy. *Macromolecules* **2008**, *41* (20), 7616–7624. https://doi.org/10.1021/ma801037q.

(49) Cohen, Y.; Albalak, R. J.; Dair, B. J.; Capel, M. S.; Thomas, E. L. Deformation of Oriented Lamellar Block Copolymer Films. *Macromolecules* **2000**, *33* (17), 6502–6516. https://doi.org/10.1021/ma000513q.

(50) Doi, T.; Takagi, H.; Shimizu, N.; Igarashi, N.; Sakurai, S. Effects of Drying Temperature in Solution Coating Process on the Structural Changes upon Uniaxial Stretching of Sphere-Forming Block Copolymer Films. *Polym J* **2020**, *52* (4), 421–433. https://doi.org/10.1038/s41428-019-0287-z.

(51) Beahan, P.; Bevis, M.; Hull, D. The Morphology of Crazes in Polystyrene. *Philosophical Magazine* **1971**, *24* (192), 1267–1279. https://doi.org/10.1080/14786437108217412.

(52) Mamodia, M.; Indukuri, K.; Atkins, E. T.; De Jeu, W. H.; Lesser, A. J. Hierarchical Description of Deformation in Block Copolymer TPEs. *J Mater Sci* **2008**, *43* (22), 7035–7046. https://doi.org/10.1007/s10853-008-3030-2.

(53) Kruse, R. L. Crazes in Osmium Teroxide Stained Styrene Polymers. *J Microsc* **1981**, *123*, 323–327. https://doi.org/10.1017/CBO9781107415324.004.

(54) Wang, C.; Wiener, C. G.; Fukuto, M.; Li, R.; Yager, K. G.; Weiss, R. A.; Vogt, B. D. Strain Rate Dependent Nanostructure of Hydrogels with Reversible Hydrophobic Associations during Uniaxial Extension. *Soft Matter* **2019**, *15* (2), 227–236. https://doi.org/10.1039/C8SM02165A.

(55) Ilavskya, J.; Jemiana, P. R. Irena: Tool Suite for Modeling and Analysis of Small-Angle Scattering. *J. Appl. Crystallogr.* **2009**, *42*, 347–353.